Experimental assessment of damage-thermal diffusivity relationship in unidirectional fibre-reinforced composite under axial tensile test

Jalal El Yagoubi, Jacques Lamon, Jean-Christophe Batsale, Marion Le Flem

Version of Record: https://www.sciencedirect.com/science/article/pii/S1359645419302848
Manuscript_31658c8a30cb286921e7f8e325923160

Experimental assessment of damage-thermal diffusivity relationship in unidirectional fibre-reinforced composite under axial tensile test.

Jalal El Yagoubi[b,1,*], Jacques Lamon[c,a], Jean-Christophe Batsale[b], Marion Le Flem[d]

[a] *Laboratoire des Composites Thermostructuraux, UMR 5801*
Bordeaux University, 33600 Pessac, France
[b] *Univ. Bordeaux, I2M, UMR 5295, F-33400 Talence, France*
CNRS, I2M, UMR 5295, F-33400 Talence, France
Arts et Metiers ParisTech, I2M, UMR 5295, F-33400 Talence, France
[c] *LMT, CNRS/Ecole Normale Supérieure Paris-Saclay/University Paris-Saclay*
61 avenue du Président Wilson
F-94230 Cachan, France
[d] *Cea Saclay*
91191 Gif-sur-Yvette, France

Abstract

The influence of damage on thermal properties is an important issue for the design of reliable ceramic matrix composites for high temperature applications. This work is devoted to the experimental study of this influence on SiC/SiC minicomposite. This single tow reinforced composite is appropriate to investigating the damage mechanisms and thermal behavior. Relationships between the properties of constituents (fibre / matrix / interface) and behavior of the assembly can be established. Nevertheless, the literature review showed that no experimental study has focused on the thermal behavior during mechanical tests. Lock-in thermography was used to measure the thermal diffusivity during tensile tests on minicomposites while acoustic emission technique allowed monitoring damage. In this work, it is demonstrated that the evolution of the thermal diffusivity competes favorably with acoustic emission and Young's modulus as a reliable indicator of matrix damage.

Keywords: Damage, Diffusivity, Composite, Fracture, Ceramics, Thermography

*Corresponding author. Tel.: +33-(0)-556-845-842
Email address: jalal.el-yagoubi@lcts.u-bordeaux1.fr (Jalal El Yagoubi)

1. Introduction

Damage - thermal diffusivity relationship is a crucial issue for both structural health monitoring and thermal design of ceramic matrix composites. For more than a decade, SiC/SiC Ceramic Matrix Composites (CMC) have been investigated with a view to use in nuclear reactors of new generation as refractory fuel cladding. This structural element should combine mechanical strength, resistance to irradiation and oxidation, and high thermal conductivity [1–5]. The SiC/SiC shell must contain the fuel and transmit the large amount of heat produced by the nuclear reaction, under severe operating conditions (temperature, loading, irradiation). Ceramic Matrix Composites possess properties that are particularly attractive for structural applications at high temperatures. Although they consist of ceramic constituents, they exhibit a damageable elastic behavior and much higher toughness than bulk ceramics. Damage results from cracks located in the matrix and at fibre/matrix interfaces and causes disruption of heat transfer and degradation of thermal conductivity. Thus, the evolution of thermal properties with damage becomes a critical issue.

The local disturbances induced by cracks are revealed by infrared imaging. Thermal contrasts are potentially used in non-destructive testing of composites to detect delamination cracks in laminates [6], debonding in composite adhesive joints [7, 8] or in impact damage [9, 10]. Infrared thermography was also used to detect the damage and the chemical changes caused due to localised heat exposure [11]. In [12, 13] the crack growth is measured during a Compact Tension test using the local thermal variations. Hence, infrared imaging is largely used as a Non Destructive and Evaluation Technique. Instead of focusing only on the thermal contrasts, one can investigate the evolution of the thermal properties such as the diffusivity and conductivity. Work on unidirectional composites (SiC/RBSN [14], Nicalon SiC/MAS [15]) and on laminated composites [16] has clearly demonstrated the effect of interfacial cracks on thermal diffusivity . The experimental results reported in [17–19] for multidirectional reinforced composite, showed that measurements of thermal diffusivity during mechanical test monitor the progression of damage. McDonald [15, 20], and Dry-

den [21–23] proposed investigations and analyses of the thermal conductance / resistance of matrix and interface cracks as a function of crack opening displacement. The relation with applied stress and strain was not established except in McDonald [15] where an experimental plot of thermal diffusivity versus tensile stress was reported for an unidirectional Nicalon/MAS composite.

The mechanical behavior of CMCs and damage phenomena are well known in the literature [24–28]. However, the relationship between the degradation of thermal properties and damage evolution has not been established experimentally. Thus, the intent of the present paper is to tackle this problem by investigating the influence of damage modes on the thermal diffusivity of unidirectional composite (minicomposite) during uniaxial tensile tests. The interest of minicomposites for the investigation of microstructure-property relations has been well demonstrated in numerous studies [28, 29]. First, from a practical point of view, the control of elaboration conditions (matrix infiltration) is not as complex as for multidirectional reinforced composites (2D, 2.5D and 3D). Then, the behavior of damaged woven composite is dictated by the longitudinal tows, which is reproduced in minicomposites [30]. Hence, minicomposite behavior has been studied extensively; This has enabled the understanding and modeling of matrix cracking and multiple fibre breaks in [26, 28] and static fatigue behavior in [31, 32]. However, no experimental study has focused previously on the thermal behavior of minicomposite under tensile load. A previous paper combined micromechanics-based equations of matrix multiple cracking and equations of heat transfer in the vicinity of cracks to end up with thermal conductivity-deformation relation [33]. The present paper proposes an original experimental approach based on a combination of various techniques for monitoring of damage and thermal behavior of minicomposites during tensile tests. Finally, thermal and mechanical behaviors of minicomposites are compared in order to deduce the relationship between damage and changes in thermal diffusivity.

2. Minicomposite

Minicomposite test specimens (Fig. 1) were made of single yarns consisting of 500 commercial silicon carbide fibres, a Pyrocarbon (PyC) interphase of few tens of nanometres,

and a silicon carbide matrix deposited via Chemical Vapor Infiltration (SiC CVI). Matrix thickness ranged from 2-3 μm at the core to 8-10 μm at the rim. Figures 2 and 3 show porosity inherent to the CVI process of matrix deposition. Image analysis of polished sections (Fig. 2.b) was used for the determination of specimen cross section areas as well as the fractions of fibre (V_f) and matrix (V_m).

Two batches of minicomposites were prepared:

M1 : reinforced by *Hi-Nicalon S* commercial fibres (Nippon Carbon Ltd);

M2 : reinforced by *Hi-Nicalon* commercial fibres (Hi-Ni) (Nippon Carbon Ltd);

The main properties of SiC fibres are given in Tab. 1, and the characteristics of minicomposite test specimens are given in Tab. 2.

3. Experimental

The experimental setup (Fig. 4) has been developed in order to study simultaneously the thermal and mechanical behaviors of minicomposite. Minicomposites under load were heated using a laser beam while the thermal response was recorded using an Infrared camera. Acoustic emission technique was used for damage monitoring. It gives real-time information on initiation and evolution of damage. It was also useful to check that damage did not grow during the measurement of the thermal diffusivity when the load was kept constant. In the following, the experimental setup is described in detail.

3.1. Tensile tests

Tensile tests were performed using an electromechanical testing machine (MTS). Metallic cylindrical tabs were glued at both ends of specimens. The spacing distance (gauge length) was 30 mm. Specimens strain was derived from the displacement of the upper crosshead using two inductive sensors (LVDT) for checking specimen straightness and grips alignment. A compliance calibration technique was used in order to estimate the deformation of grips that was subtracted from crosshead displacement ($\mathrm{Cs} = 0.3\ \mu m.N^{-1}$) [34]. Tensile tests were carried out under quasi-static conditions with a crosshead displacement rate of 0.05mm/min. The crosshead displacement was kept constant during thermal measurements.

3.2. Damage characterization

An acoustic emission sensor (*Pico* sensors from Euro Physical Acoustic) was placed on each machine grips. Acoustic emission events with an amplitude higher that the threshold (40dB) were recorded during entire test, i.e during loading-unloading at constant rate as well as during the thermal diffusivity measurement under constant load. Then, the samples were observed after failure in a Scanning Electron Microscope, using backscattered electron imaging, in order to count the number of matrix cracks and measure crack spacing distance.

3.3. Thermal diffusivity measurement

The measurement of thermal conductivity presents several difficulties which lie mainly in the determination of heat flux. On contrary, unsteady thermal conditions allow the estimation of thermal diffusivity from temperature evolution during transient heat transfer. Thus, as discussed below, analysis of thermal characteristic time periods is needed to guide experimental choices. Indeed, heat transfer must take place within a time window consistent with the experimental device. In this work, an Infrared camera was used for acquiring thermal signals at a frequency of a few hundreds hertz.

Dimensionless fourier number (Fo) depends on thermal diffusivity (a_c) , characteristic time (t_c) and characteristic length (d_c):

$$Fo = \frac{a_c.t_c}{d_c^2} \tag{1}$$

When $Fo = 1$, t_c is the time period during which heat passes through a medium of thickness d_c and thermal diffusivity a_c. It indicates the time period for measurement of transient thermal properties.

In fibre direction (longitudinal), characteristic length is centimeter-scale and thermal diffusivity of the order of tens of $\mathrm{mm}^2 s^{-1}$, so that characteristic time period is 10s (Tab 3). On the other hand, characteristic time in transverse direction (perpendicular to fibres) is of the order of one microsecond (Tab. 3). For this latter time scale, specific tools are required

(e.g. IR monodetector with a high frequency acquisition rate or heterodyne method for periodic signals [35]). It thus appears that only the estimation of longitudinal thermal diffusivity was possible using unsteady thermal conditions. Periodical conditions are suitable for thin samples for which the transient is short.

The retained method was initially proposed by Angström [36] and adapted subsequently by several authors [37–40]. It consists in creating a local oscillating heat source in the material and to process the temperature profile along the axial direction. When periodical steady state is reached, a damped thermal wave out of phase propagates through the solid medium. The estimation procedure of longitudinal thermal diffusivity, detailed in the next section, is based on the evaluation of the damping and phase shift.

The local modulated heat source is provided by a laser beam of 532nm wavelength emitted by a diode (1 Watt). The later is powered by a signal generator that produces sine waves at the selected frequency. Then, the laser beam passes through a lens to be focused so that the spot size be as small as possible. A spot size of about 100μm at the surface of specimen was sought. However, a more precise determination of the spot size was not possible. A heat point-source can be reasonably assumed. The thermal excitation system (diode and lens) was mounted on a three axe-precision positioning stage in order to acurately control the spatial position of the spot on the specimen and the lens focus. Thus, a heat source was generated at the center of the minicomposite placed in the grips of the tensile machine.

An infrared camera (Titanium 520M from FLIR) captures the infrared signal (IR) emitted by the outer surface of specimen. It has 320x256 InSb sensors and is equipped with a 50mm objective with an extension ring to reduce spatial resolution to a size of about 80 μm. Infrared images are recorded at 100Hz. Then a dedicated software (Altair-LI also supplied by FLIR) is used to compute maps of damping and phase shift. It is worthnoting that the reference phase is assumed to be given by the signal generator that is connected to the appropriate Lockin input of the camera. Infrared signal processing to estimate thermal diffusivity, is detailed in the next section.

It should be noted that the exact shape of the spot and the amount of energy absorbed by the material do not affect the estimation of the thermal diffusivity. On the contrary,

the signal to noise ratio and the periodicity (pulsation) of the heat source are playing an important role.

4. Infrared signal processing

4.1. Equations

In 1861, Angström [36] measured the thermal diffusivity of a long and homogeneous isotropic metallic bar. A periodic sinusoidal heat flux was generated, temperature was measured at the surface. Assuming one-dimensional heat transfer, this experiment can be described by the partial differential equation in Eq. 2 with the boundary and initial conditions given in Eq. 3:

$$\frac{\partial^2 T}{\partial x^2} - \frac{hp}{\lambda_x S} T = \frac{1}{a_x} \frac{\partial T}{\partial t} \tag{2}$$

Where h is the convective heat transfer coefficient, p is the perimeter, S is the cross-sectional area, λ_x and a_x are respectively longitudinal thermal conductivity and diffusivity.

$$\begin{aligned} t = 0 \qquad & T(x,t) = 0 \\ x = 0 \qquad & -\lambda_x \frac{\partial T}{\partial x} = \phi_o + \Delta\phi_o sin\left(\omega t + \varphi_o\right) \\ x \to \infty \qquad & T(x,t) = 0 \end{aligned} \tag{3}$$

The local heat flux is described by the following quantities: ϕ_o is the offset, $\Delta\phi_o$ is the amplitude, ω is the pulsation and φ_o is the reference phase.

In the periodic steady state, the solution $T(x,t)$ of Eq. 2 is then expressed as the sum (Eq. 4) of a steady component, noted $\overline{T}(x)$ and a periodic component, noted $T^*(x,t)$ with a pulsation ω imposed by the heat flux at x =0.

$$T(x,t) = \overline{T}(x) + T^* \tag{4}$$

For the purpose of thermal diffusivity identification, one focuses only on the periodic components given in Eq. 5:

$$T^* = A(x) cos\left(\omega t + \varphi(x)\right) \tag{5}$$

The amplitude and the phase difference of the wave are respectively given by Eq. 6 and Eq. 7:

$$A(x) = A_o exp\left(-z_r x\right) \tag{6}$$

$$\varphi(x) = \varphi_o - z_i x \tag{7}$$

where z_i and z_r are as follows (Eq. 8, Eq. 9):

$$z_i = -\frac{\partial \varphi(x)}{\partial x} = \sqrt{\frac{1}{2a_x}\left[\sqrt{\left(\frac{hp}{\rho C_p S}\right)^2 + \omega^2} - \frac{hp}{\rho C_p S}\right]} \tag{8}$$

$$z_r = -\frac{\partial \ln\left(A(x)\right)}{\partial x} = \sqrt{\frac{1}{2a_x}\left[\sqrt{\left(\frac{hp}{\rho C_p S}\right)^2 + \omega^2} + \frac{hp}{\rho C_p S}\right]} \tag{9}$$

The product of terms (z_i, z_r) is denoted z_π and given by the following equation (Eq. 10):

$$z_\pi = z_i . z_r = \frac{\omega}{2a_x} \tag{10}$$

Then, for several experiments conducted at different pulsations (k experiments), the previous scalar equation (Eq. 10) turns to a vectorial expression (Eq. 11):

$$\underline{Z_\pi} = \frac{1}{2a_x}\underline{\Omega} \tag{11}$$

where $\underline{\Omega}$ and $\underline{Z_\pi}$ are the vectors associated to ω and z_π.
Finally, longitudinal thermal diffusivity is calculated using the least squares method [40]:

$$a_x = \frac{1}{2(\underline{\Omega}^T \cdot \underline{\Omega})^{-1} \cdot \underline{\Omega}^T \cdot \underline{Z_\pi}} \tag{12}$$

It is worth noting that Eq. 12 was developed on a homogeneous material [40]. The implementation of the method was first validated on homogeneous reference materials: Alumium oxide ($9.2 mm^2.s^{-1}$) and AXF-5Q poco graphite ($67 mm^2.s^{-1}$). The particular case of the estimation of a damaged minicomposite is discussed in the next section.

4.2. Particular case of damaged minicomposite

Heterogeneity through the section

It is worth pointing out that given the geometry and the properties of minicomposites, the Biot number is $Bi = \frac{hL}{\lambda_x} \approx 10^{-5}$ (with h=$10W.m^{-2}.K^{-1}$) which validates the assumption of onedimensional heat transfer, reasonably far from the local heat source (about two times the diameter).

The first issue to be addressed is the heterogeneity through the cross-section. The minicomposite may be represented, at first approximation, as a wire (representing the SiC fibres bundle) embedded in SiC-CVI matrix. This simplified model was used to perform virtual experiments using finite element analysis. The partial diferential equation Eq. 2 was solved using the FlexPDE software in the axisymmetric domain defined in Fig. 5 a with the following boundary and initial conditions:

- A modulated heat source was located at segment OA of the outer surface (Laser);
- Convective heat flux was prescribed at segment AB of the outer surface (with $h = 10W.m^{-2}.K^{-1}$);
- At $x = L$, the temperature was set to $T = 0$;
- At $x = 0$, symmetry condition was prescribed;
- At initial time, temperature in the whole domain was set to zero.

Numerous virtual tests were performed for excitation frequencies ranging from 0.5Hz to 45Hz. The temperature along the segment AB was considered to be the signal recorded during the experiment. Then, the amplitude profile ($\varphi(x)$) as well as the phase shift profile ($A(x)$) were derived from the simulated temperature. The thermal diffusivity obtained using Eq. 12 is plotted, as a function of the excitation frequency, on Fig. 6a.

The numerical results are, hereafter, interpreted using the ratio of diffusion length $L_p = \sqrt{\frac{a}{\pi f}}$ to minicomposite radius (Fig. 6b).

Fig. 5 .b and Fig. 5 .c describe the two asymptotic behaviors that can be identified on Fig. 6a and Fig. 6b:

- For excitation frequencies smaller than 10Hz, the diffusion length is larger than minicomposite radius. As depicted by the isotherms in Fig. 5 .b, heat propagated through the section and, far from the local heat source, heat transfer is one-dimensional. The asymptotic value (for $f \to 0$) of thermal diffusivity is equal to the diffusivity obtained by the mixture law.

- For frequencies larger than 35Hz, the thermal diffusion length is smaller than minicomposite radius. Thus, the thermal wave remains superficial (Fig. 5c) and the asymptotic thermal diffusivity (for $f \gg 35$Hz) is close to that of the matrix.

This simple model does not account for the complexity of heat transfers occuring in the minicomposite. In particular, it does not consider (1) the spatial distribution of fibres and (2) the presence of an interphase between the fibres and the matrix. Yet, the virtual tests give useful guidelines for experimental choices. Thus, this analysis showed that the excitation frequency domain is an important parameter that needs to be carefully examined. Indeed, at frequencies larger than 10Hz, the estimated thermal diffusivity is different from the apparent one. In this work, experiments were conducted for frequencies ranging from 0.1Hz to 5Hz.

Heterogeneity in the longitudinal direction

When cracks appear in the matrix, the temperature field is disturbed, and heat transfer is no longer one-dimensional. Then, the significance of this local disturbance needs to be evaluated with respect to crack opening displacement (COD). First, spatial resolution of the camera (about 100μm) was two orders of magnitude larger than COD (about 1μm). This means that the local disturbance cannot be detected by the IR camera. Second, the characteristic diffusion length (L_p) is several orders of magnitude larger than the COD. Matrix cracking can therefore be seen as a diffuse damage.

Hence, it was shown that the equivalent material based approach holds for the damaged minicomposite. Finally, the apparent longitudinal thermal diffusivity of minicomposite $a_x(\varepsilon)$ can be estimated using Eq. 12 for different applied strains (ε).

5. Results and discussion

5.1. Tensile behavior

The tensile stress-strain curves (Fig. 7) exhibit the elastic damageable behavior of CMCs reported in previous papers [26–31]. They display the following features at increasing stress which can be attributed to both basic damage mechanisms of matrix cracking and associated fiber/matrix debonding, on the basis of previous experimental and modeling works on the behavior of minicomposites and composites.

- at strains smaller than 0.1%, an initial linear elastic domain.
- at strains between 0.1% and 0.3%, a non linear domain with upward curvature indicative of increasing compliance, resulting from transverse matrix cracking and associated fiber/matrix debonding.
- at a strain about 0.3%, an inflexion point that marks a transition in the damage process from matrix cracking that saturated to a less severe process such as extension of debonding,
- at strains comprised between 0.3% and about 0.4% for HNS/SiC a non linear domain resulting from extension of debonding. This domain was less noticeable for Hi Nicalon/SiC.
- at strains comprised between 0.4% and about 0.7% for Hi Nicalon S/SiC (0.3 <strain<0.7% for Hi Nicalon/SiC) a second linear domain indicative of constant compliance, that is attributed to deformation of fibres and sliding in the presence of complete debonding.
- and at strains $> 0.7\%$, a non linear domain with upward curvature, indicative of fibre failures. Note that for the Hi-Nicalon S/SiC minicomposite, this domain did not appear on figure 7 due to premature ultimate failure.

Loading-unloading cycles during tensile tests were performed in order to determine Young's modulus changes during tensile tests and interface characteristics. On reloading, the elastic response of the damaged composite is shown by the linear upper portion of the cycle when both the matrix and the fiber deform without sliding. This line intercepts the origin for the Hi Nicalon/SiC composite, which indicates the presence of negligible thermally induced residual stresses. By contrast, the line for Hi Nicalon S /SiC intersects the strain axis at a negative strain value which indicates more significant residual stresses. These results agree with the residual strain values observed after unloading (Figure 7). Figure 8 shows elastic modulus decrease during damage, which illustrates the progressive decay of contribution of the matrix to load sharing. At strains $> 0.4\%$ the elastic modulus approaches the value given by the mixture laws when the load is carried by the fibers only (Tab. 5):

$$E_c = \frac{E_f V_f}{E_o} \tag{13}$$

The hysteresis loops illustrate sliding and friction of the fiber and the matrix in the debonded interfaces. Opening width of loops together with residual strains after unloading reflect the contribution of interface in load transfer. They are both larger in the presence of long debonded interfaces and small interface shear stress. These trends can be quantified by the value of interfacial shear stress that can be derived from loop width [41] or using the following equivalent expressions that are easier to handle [24, 42, 43] and that gave close results:

$$\tau = \frac{\sigma_s R_f}{2V_f l_s(1 + \frac{E_f V_f}{E_m V_m})} \tag{14}$$

$$\tau = \frac{\sigma_s R_f V_m}{2V_f l_s} \tag{15}$$

where E_m is the matrix Young's modulus, E_f is the fiber one, V_m and V_f are the volume fractions of fibre and matrix, and R_f is the fiber radius, l_s is the spacing distance of the matrix cracks at saturation and σ_s is the corresponding stress. The l_s was measured by microscopy. In section 5.2.1, Figure 11 shows the distributions of measured ls. The interfacial shear stress τ is a useful characteristic of interface efficiency in the post crack deflection behavior

of composites. It varies inversely with interface crack size (l_d), according to the following classical equation:

$$l_d = \frac{\sigma k R_f}{2V_f(1+k)\tau} \tag{16}$$

where σ is the applied stress and $k = \frac{E_m V_m}{E_f V_f}$.

Tab. 4 gives the values of τ obtained for the minicomposites. The τ values indicate that the interphase of Hi Nicalon/SiC was stronger than that of Hi Nicalon S/SiC, which implies that the debonded interfaces were larger in the Hi Nicalon S/SiC minicomposites. Which may explain why the non linear domain identified after matrix cracking saturation was less marked for Hi Nicalon/SiC. Indeed, it can be logically expected that the extension of interface cracks is smaller for short cracks and stronger interfaces. Interphase strength may be related to interphase thickness that was larger in Hi Nicalon S/SiC minicomposites. Finally, the main material's features derived from the tensile tests are summarized in Tab. 4.

5.2. Damage characterization

5.2.1. Microscopy

Scanning Electron Microscopy images show matrix cracks perpendicular to fibre direction after minicomposite failure (Fig. 10 and Fig. 11). These cracks are randomly distributed (Fig. 8). The statistical distribution of the measured crack spacing distances exhibits a gaussian distribution. In the case of the minicomposite *M1*, the average crack spacing distance is 376 μm and the standard deviation is 167 μm. The material *M2* exhibits a higher crack density, the average crack spacing distance is 128 μm and the standard deviation is 43 μm. Then, one can derive the ultimate number of cracks (N_s) from the average crack spacing distance ($\langle \Delta L \rangle$) according to Eq. 17. Hence, after matrix cracking saturation, the total number of cracks is equal to 79 for *M1* and 234 for *M2*.

$$N_s = \frac{L - \langle \Delta L \rangle}{\langle \Delta L \rangle} \tag{17}$$

Where L is the minicomposite's length (L=30mm).

5.2.2. Analysis of acoustic emission

Fig. 12 depicts the evolution of the normalized cumulative energy during tensile tests. It reveals the four domains that have been identified on the stress-strain curves:

- First, there was no acoustic emission at low strains below 0.08% for minicomposite *M1* and 0.04% for minicomposite *M2*, which indicates elastic deformations;
- The steady acoustic activity in the second part (strains ranging form 0.1% to 0.3%) of the curve can be attributed to matrix cracking. It did not include fibre failures, as suggested by previous works [28, 30].
- In the non linear part, at strains between 0.3% and 0.4%, acoustic emission activity decreased, indicating a less severe process. Note that this domain is more noticeable on the stress-strain curve of the Hi-Nicalon SiC.
- In the fourth part beyond 0.4% of strain, the acoustic activity is also steady but much less intense.

Fig. 12 shows that there was no acoustic emission during the loading-unloading cycles (Kaiser effect) when fibre sliding occurs. Thus, the acoustic activity identified in the fourth domain can be attributed reasonably to fiber failures or unidentified sources.

5.3. Thermal diffusivity

Thermal diffusivity was estimated under constant load during the tensile tests while acoustic activity was continuously recorded. The plots of cumulative number of counts clearly show that damage did not grow during the thermal characterization. The plots of thermal diffusivity data reveals three of the domains that have been identified above (Fig. 13).

- At low strains (<0.1%) corresponding to elastic deformations, thermal diffusivity was constant.This indicates that there was no disturbance, as expected with elastic behavior. Then, this shows that elastic deformations do not affect thermal diffusivity.

- Under higher strains ($< 0.4\%$) thermal diffusivity decreased by 15% for minicomposite *M1* and by 35% for *M2*. This corresponds to the domain of matrix cracking and crack extension that occurs in this deformation range, as suggested by stress-strain behavior and acoustic emission.

- At strains $> 0.4\%$, thermal diffusivity was constant. This suggests that new causes of disturbance did not appear. This is in agreement with the phenomena attributed to this domain of deformation (i.e deformation of fibres and fibre sliding) that do not increase damage. Nevertheless, it is worth noting that the measurement of diffusivity was not possible at strains close to ultimate failure because of instability at the end of the test.

The respective minimum values of thermal diffusivity at strains between 0.4 and 0.7% are 9.4 mm^2s^{-1} for Hi Nicalon S/SiC minicomposites and 4.0 mm^2s^{-1} for Hi Nicalon/SiC minicomposites. It is important to point out that these values coincide satisfactorily with the values of thermal diffusivity of Hi-NicalonS and Hi Nicalon fibers respectively (Tab. 1). This result is consistent with the interpretation of the stress-strain behavior at the same range of strains, i.e. that the fibers were completely debonded. Note that this interpretation is supported by previous experimental and modeling works (see for instance [28, 31]) that showed that the load is carried by the fibers only beyond saturation strain. Noting that fiber diffusivity is the theoretical lower bound for damaged composite diffusivity, it can be inferred from diffusivity measurements that the contact between the fiber and the matrix did not allow sufficient heat transfer and constriction.

Moreover, Fig. 14 shows that in the cracked material, the profiles of amplitude and phase difference do not display local disturbances. Thus, damage was homogeneously distributed along the fibre direction, as it was also observed by electron microscopy.

5.4. Relationship between damage and thermal diffusivity

In Fig. 15, the relative diffusivity (Eq. 18) is compared to acoustic emission (Eq. 20) and elastic modulus data (Eq. 19) for deformations up to 0.65%. The agreement in data indi-

cates that elastic modulus, thermal diffusivity and acoustic emission counts are equivalent indicators of matrix crack density.

$$d_a = \frac{a(\varepsilon)}{a_0} \tag{18}$$

$$d_E = \frac{E(\varepsilon)}{E_0} \tag{19}$$

$$d_{AE} = \frac{c(\varepsilon)}{c(\varepsilon_{sat})} \tag{20}$$

where a_0, E_0 are the initial thermal diffusivity and elastic modulus, c is the cumulative energy, and ε_{sat} is the strain at matrix cracking saturation (0.4%).

Fiber failures were not expected because the deformation range was below 0.65% as indicated above. It was difficult to monitor the evolution of thermal diffusivity for strains higher than 0.65% because of the instability in the tensile behavior due to fibre breakage above 0.7%. The elastic modulus decreased after saturation of matrix cracking, while the diffusivity remained constant in this deformation range. It appears that matrix cracking only was detected by thermal diffusivity measurement, although other phenomena were evidenced by elastic modulus decrease, residual deformations increase and acoustic emission. At strains larger than the matrix crack saturation strain, the result that the value of composite diffusivity equal to the lower bound value given by fiber diffusivity, implies that there was negligible heat transfer through the interface cracks. As a consequence, it can be deduced that the constriction of heat flux lines in the fibers was negligible. This trend is in agreement with the stress strain curves which indicated that, at strains above the matrix cracking saturation strain, fiber debonding was complete: $2n_s l_d = L_0$, where n_s is the number of cracks at saturation, l_d is the debond length, L_0 is the gauge length. It can be inferred that (1) the interface crack opening displacement and the interface roughness were such that the interface crack conductance was low, and (2) the conduction of gas through the interface crack was low also. In [44], it was found that the interface crack conductance was about 1-5 $\mathrm{MW.m^{-2}.K^{-}}1$, and that it increased with interface shear stress. Values of the same order of magnitude were estimated in [15] on a SiC/MAS composite: the thermal conductance of the interface was found to decrease with increasing crack opening displacement, from an initial

value of about 0.3 to 1 MW.m^{-2}.K^{-}1. The total debond length $2n_s l_d$ (equal to L_0) is independent of the number of cracks at saturation. Therefore, the thermal diffusivity at strains above saturation strain is controlled by interface crack opening displacement and roughness, and conduction properties of the gas present in the interface crack. The former parameters depend on interface characteristics which are reflected satisfactorily by the interface shear stress [42]. Strengthened PyroCarbon interphases were obtained by functionalization of SiC fibers [45]. Interface shear stresses as high as 370 MPa were reported [42]. In the presence of strengthened interfaces, debond lengths are shorter, matrix and interface crack opening displacements are smaller, and roughness is larger [45]. At strains below the saturation stress, the total debond length ($2nl_d$, n is now the strain dependent number of cracks) depends on interface shear stress. It has been shown in [45] that $2nl_d$ is smaller when the interface is stronger (short debond length, large τ). Therefore, the diffusivity decrease should be steeper for low τ. This trend is enhanced by the interface crack thermal conductance that decreases with τ through the crack opening displacement and roughness. However, if conduction through the debonded interfaces is efficient, for instance because gas conductance is high, the composite diffusivity will be increased. Thus, both matrix and attendant interface cracks determine the diffusivity loss. The thermal conductance of the cracks decreases as the crack opening displacement increases. Results of diffusivity measurements on a unidirectional NicalonMAS composite [15] agree with the above analysis. Thus, K. R. McDonald has shown that almost complete recovery of the longitudinal diffusivity followed unloading, and essentially no change in the transverse diffusivity followed unloading. The recovery of the longitudinal diffusivity was attributed to closure of the matrix cracks. By contrast, the degradation in the interface conductance was permanent, as manifest in the lack of recovery of the transverse diffusivity.

6. Conclusion

- An experimental set up was developed in order to measure the longitudinal diffusivity during axial tensile tests on SiC/SiC minicomposites reinforced by SiC Hi-Nicalon and HiNicalon S fibers. The minicomposite test specimens were heated using a laser beam

and the thermal response was recorded using an infrared camera The evolution of damage was monitored by acoustic emission technique associated to SEM observations.. The tensile stress-strain curve displays successive steps as the applied load increases, that result from cracking of the matrix and fiber/matrix interfaces, deformations, fiber sliding, and fiber fracture.

- Thermal diffusivity was found to decrease during matrix cracking to a final minimum value at matrix crack saturation which corresponds to fiber thermal diffusivity. This implies that there was negligible heat transfer through the interface cracks at strains above the strain at matrix crack saturation. Which is consistent with features of the stress-strain and acoustic emission curves that reflect complete debonding of fibers and sliding at fibre/matrix interface. This suggests that strengthened interfaces would improve interface crack thermal conductance and would allow limited thermal diffusivity loss.

- Elastic modulus, thermal diffusivity and acoustic emission counts are equivalent indicators of matrix crack density. Diffusivity measurements provide a interesting technique for the local investigation of cracking. Further, a dynamic model of the influence of damage on thermal diffusivity would allow the contribution of interface crack thermal conductance to be measured.

Acknowledgement

This work has been supported by C.N.R.S. and CEA through a grant given to J. E.. The authors are grateful to C. Sauder for the preparation of minicomposites.

List of Tables

Table 1: Selected properties of SiC fibres (at 25^oC) from [a] [46], [b] [47] and [c] [48]

Fibres	**Hi-Ni-S**	**Hi-Ni**
Diametre (μm)	13 [a]	14 [a]
Young's modulus (GPa)	408 [a]	270 [a]
Strain to failure (%)	0.63 [a]	1.04 [a]
Density ($g.cm^{-3}$)	3 [a]	2.74 [a]
Thermal conductivity ($W.m^{-1}.K^{-1}$)	18 [b]	8 [b]
Specific heat capacity ($J.kg^{-1}.K^{-1}$)	700 [c]	690 [c]
Thermal diffusivity ($mm^2.s^{-1}$)	8.6	4.4

Table 2: Structural characteristics of minicomposites.

	Fibres	Cross sectional area (mm^2)	Vol. Fraction of fibre (%)	Vol. fraction of matrix (%)
M1	Hi-Ni-S	0.14	38	62
M2	Hi-Ni	0.23	30	70

Table 3: Magnitude of the characteristic times (t_c) associated to heat transfer in the directions parallel ($\|$) and perpendicular ($\perp$) to the fibre reinforcement (d_c and a_c are the corresponding length and thermal diffusivity).

	$\|$	$\perp$
d_c	1cm	$100\mu m$
a_c	$10\text{mm}^2 s^{-1}$	$1\text{mm}^2 s^{-1}$
t_c	**10s**	$\mathbf{1}\mu s$

Table 4: Material's properties derived from tensile tests and microstructural observations.

Minicomposite	*M1*	*M2*
Young's modulus (GPa)	395	360
Strain at the linear limit (%)	0.1	0.06
Strain at the matrix cracking saturation (%)	0.37	0.39
Strain to failure (%)	0.73	0.9
Mean crack spacing distance (at saturation) (μm)	376	128
Interfacial strength τ (MPa)	9.8	47.9

Table 5: Comparison of asymptotic ratios ($\frac{a_f V_f}{a_o}$, $\frac{E_f V_f}{E_o}$) and normalized thermal diffusivity ($\frac{a}{a_o}$) elastic modulus ($\frac{E}{E_o}$).

	$\frac{E_f V_f}{E_o}$	$\frac{E}{E_o}$ (ε=0.4%)	$\frac{E}{E_o}$ (ε=0.6%)
M1	0.39	0.48	0.39
M2	0.22	0.31	0.25

List of Figures

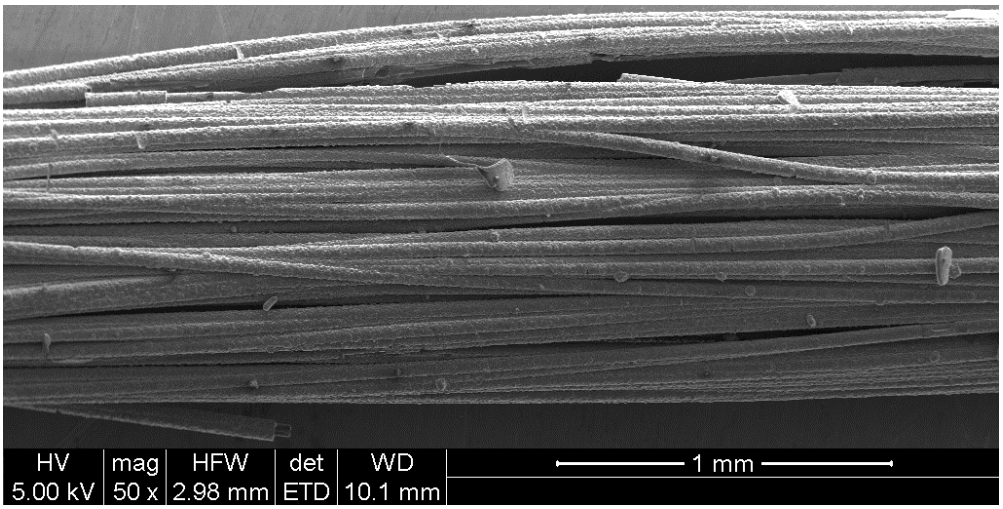

Figure 1: Overall view of SiC/PyC/SiC minicomposite elaborated by Chemical Vapour Infiltration.

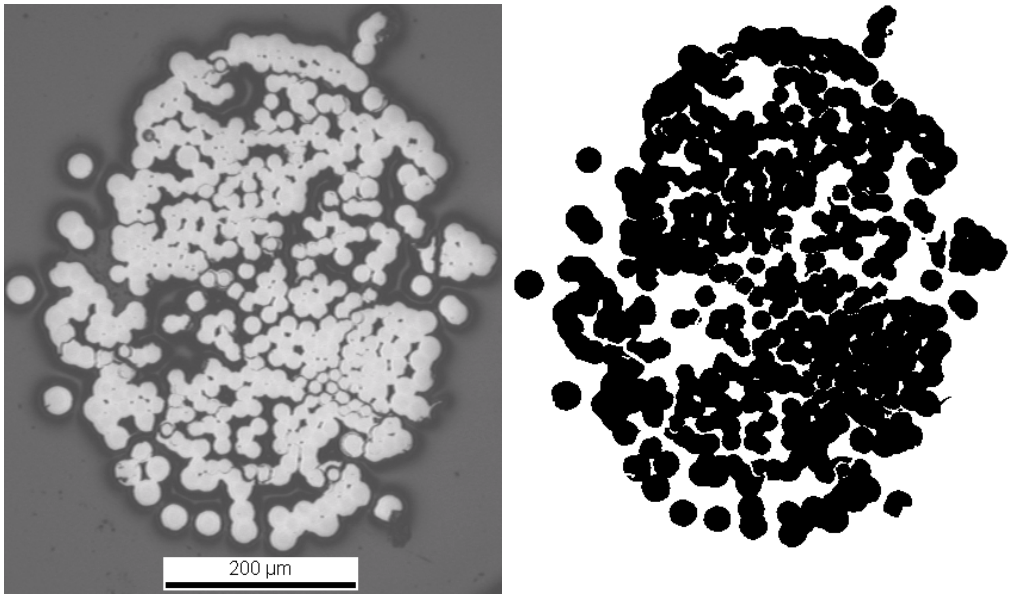

(a) (b)

Figure 2: (a) Optical image of a cross section of a SiC/PyC/SiC minicomposite elaborated by Chemical Vapour Infiltration (b) Image analysis for the estimation of the actual cross sectional area.

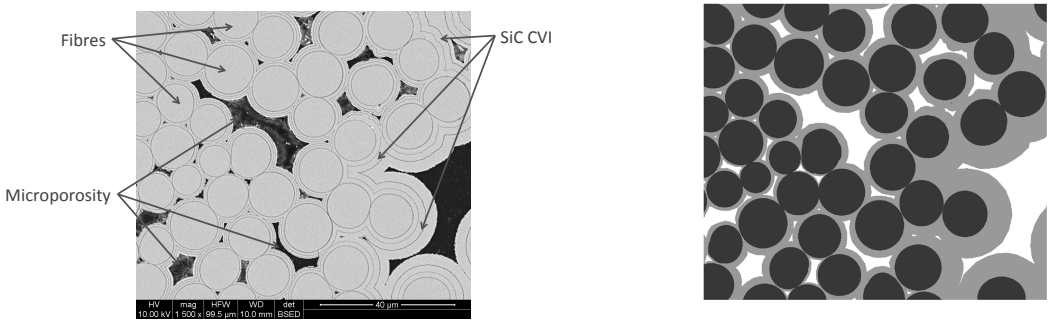

(a) (b)

Figure 3: (a) Scanning Electron Microscopy micrographs of the cross section of a SiC/PyC/SiC minicomposite showing the different phases (matrix, fibre and porosity) (b) Image analysis for the estimation of the fractions of fibres and matrix.

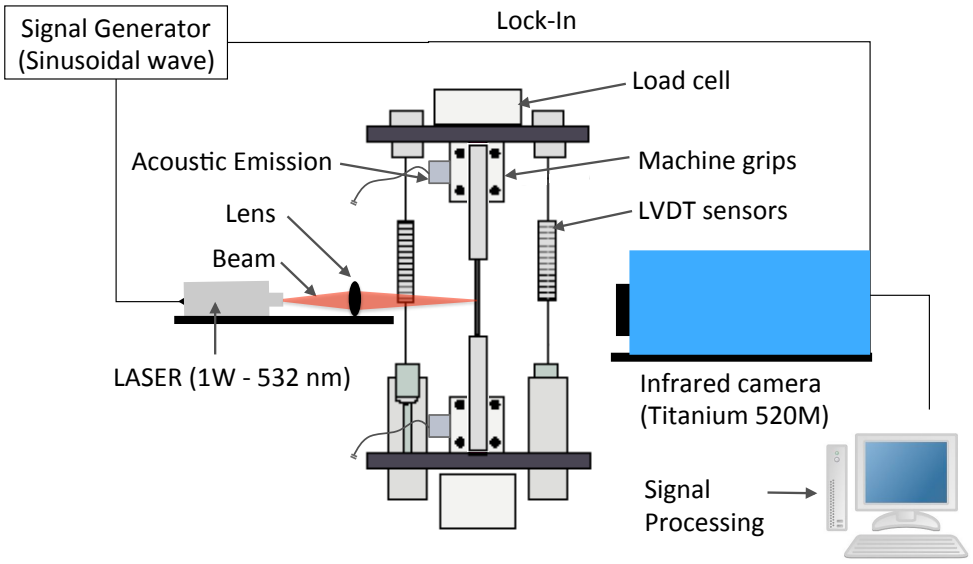

(a)

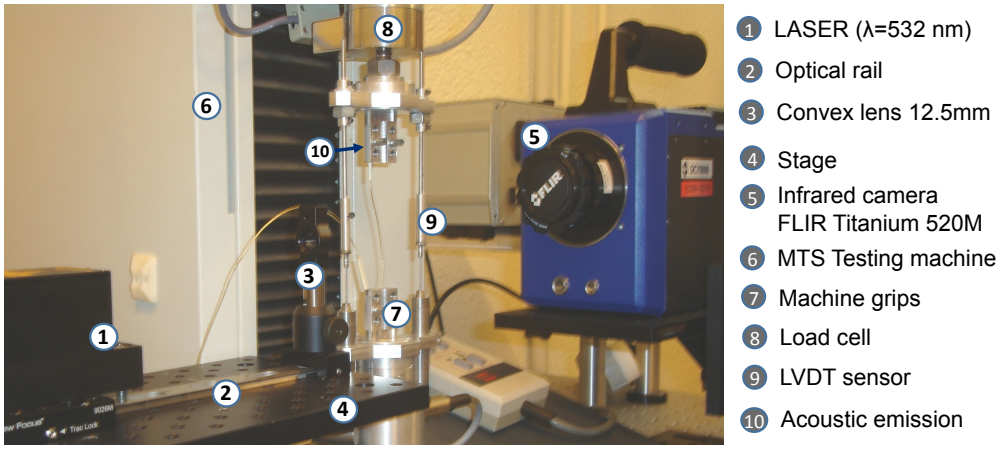

(b)

Figure 4: Experimental setup for the measurement of thermal diffusivity under axial tensile test.

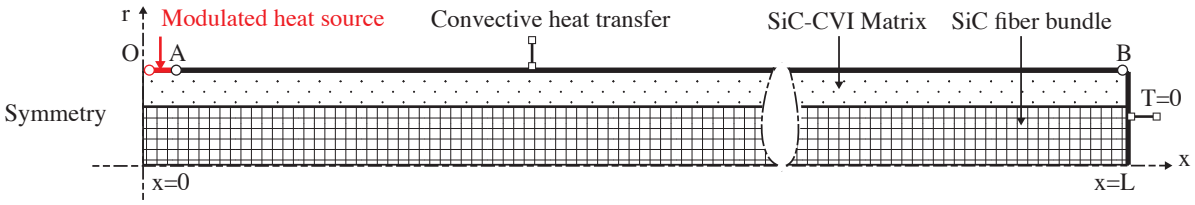

(a)

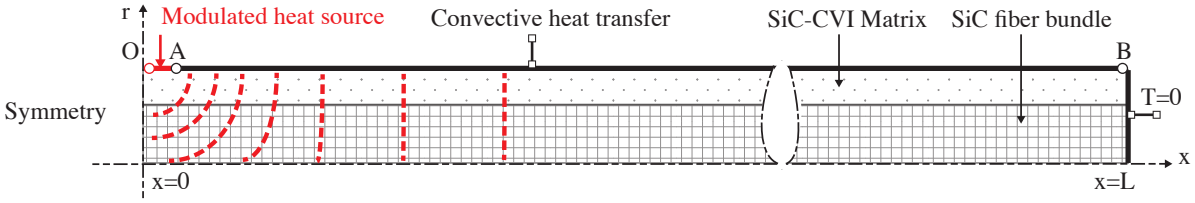

(b)

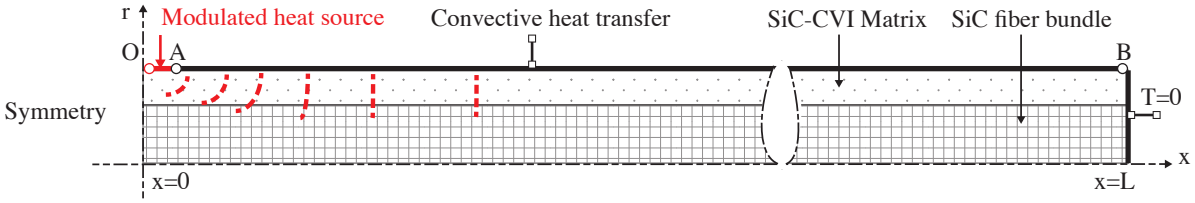

(c)

Figure 5: (a) Simplified model of minicomposite for virtual testing (thermal diffusivity measurement) using Finite Element Analysis (FLEXPDE Software). Schematic representation of isotherms for (b) frequencies smaller than 10Hz and (c) frequencies larger than 35Hz.

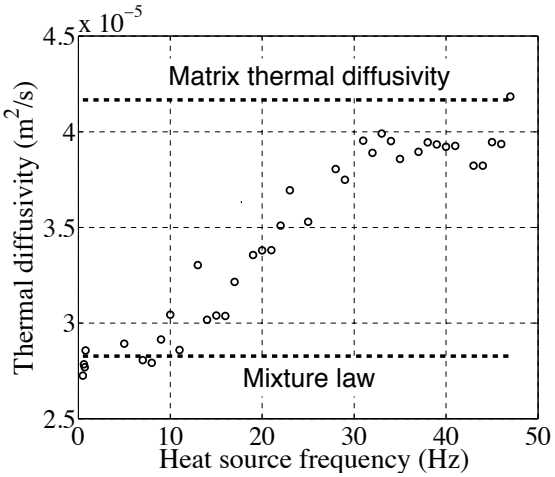

(a) Estimated thermal diffusivity.

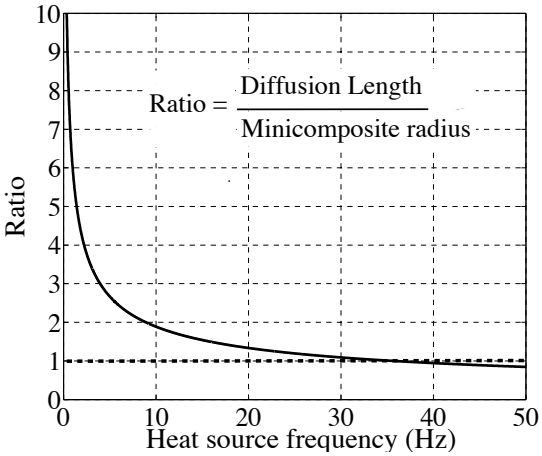

(b) Ratio of diffusion length ($L_p = \sqrt{\frac{a}{\pi f}}$) to minicomposite radius.

Figure 6: Results obtained from virtual testing of minicomposite. Influence of the local heat source frequency (LASER) on the estimated thermal diffusivity.

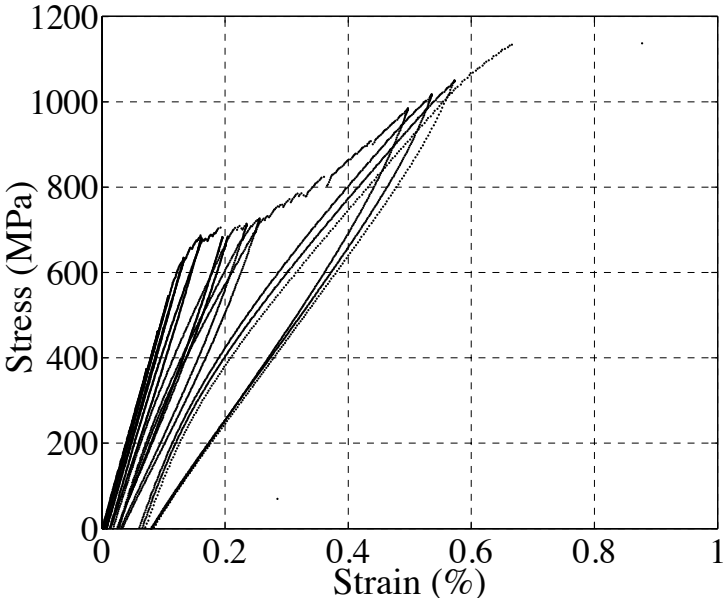

(a) M1 (Hi-Ni-S fibres)

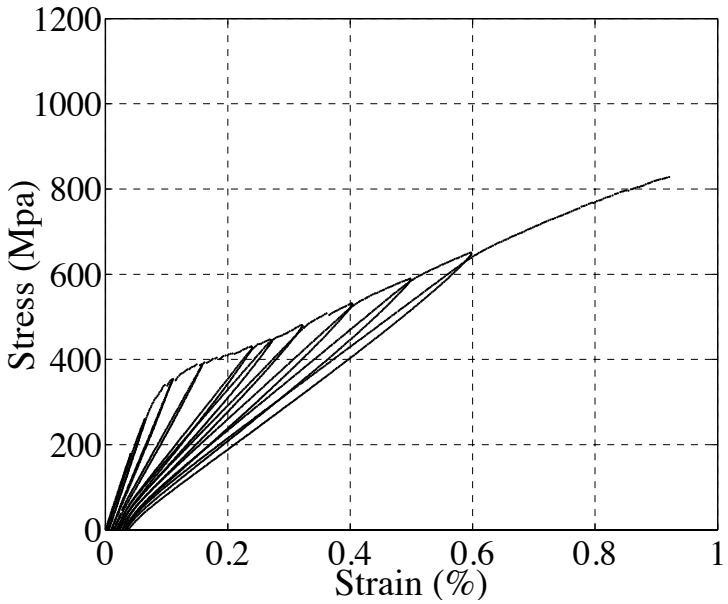

(b) M2 (Hi-Ni fibres)

Figure 7: Tensile stress-strain curves that exhibit the features of the well-known elastic damageable behavior of SiC/SiC composites.

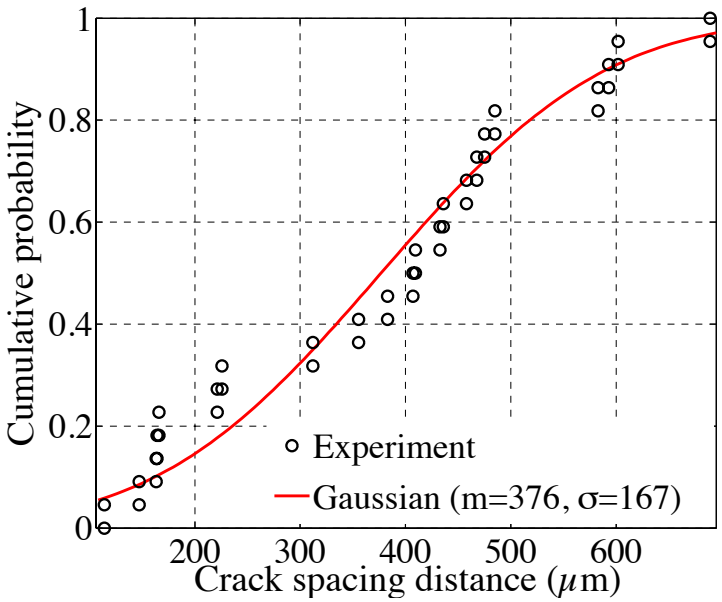

(a) M1 (Hi-Ni-S fibres)

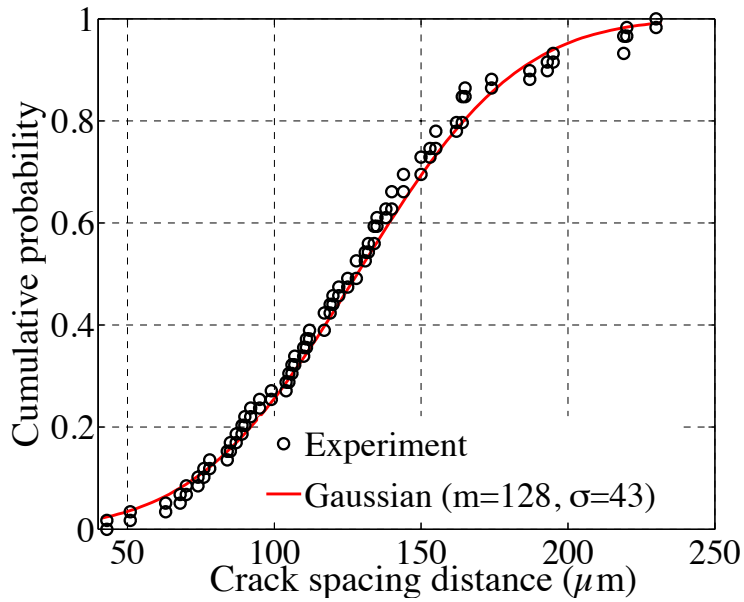

(b) M2 (Ni-Ni fibres)

Figure 8: Statistical distribution of crack spacing distances in minicomposites (after failure) measured by Scanning Electron Microscopy.

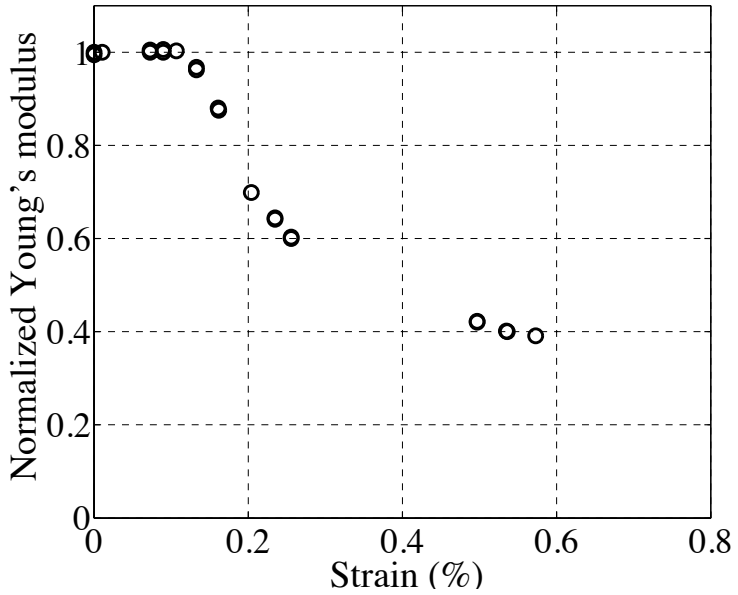

(a) M1 (Hi-Ni-S fibres)

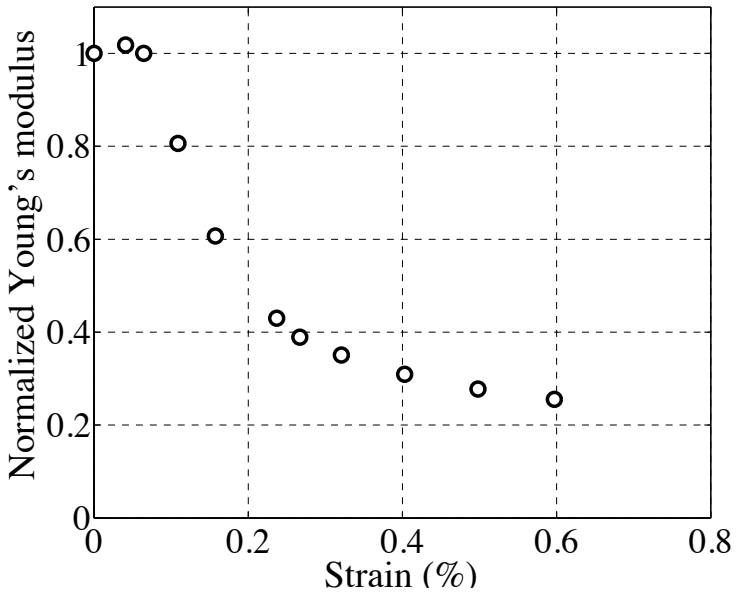

(b) M2 (Hi-Ni fibres)

Figure 9: Degradation of Young's modulus of SiC/SiC minicomposites extracted from loading-unloading cycles during axial tensile tests.

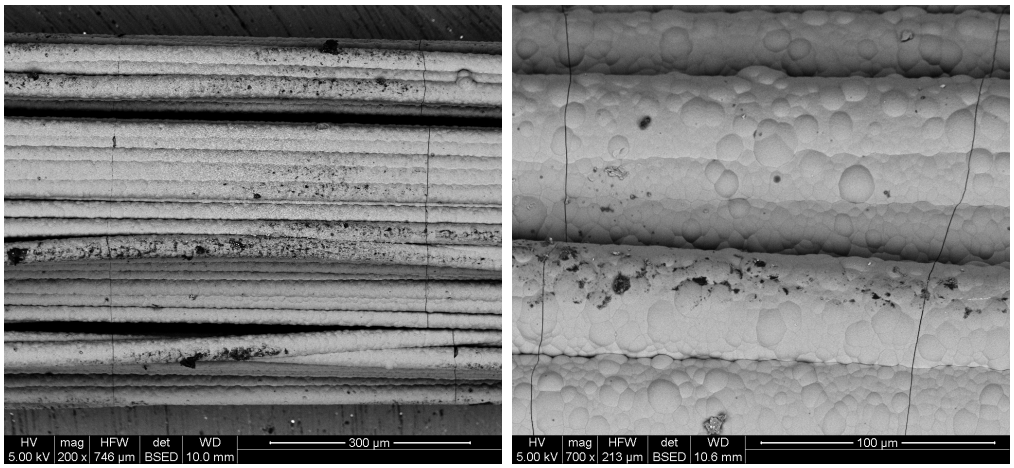

(a) M1 (Hi-Ni-S fibres) (b) M2 (Hi-Ni fibres)

Figure 10: Scanning Electron Microscopy micrographs showing matrix cracks perpendicular to fibre direction, after minicomposite failure.

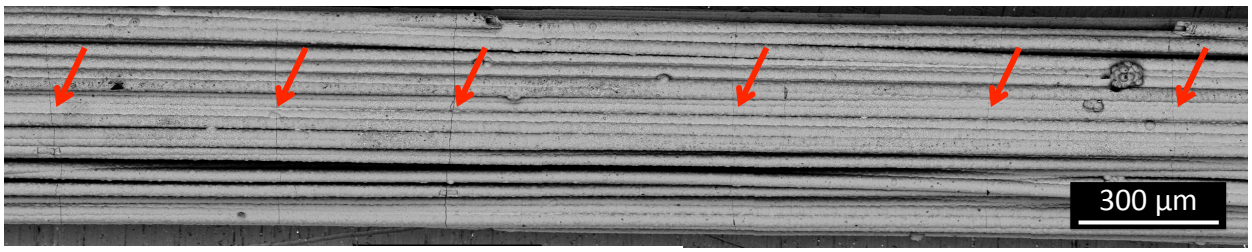

Figure 11: Scanning Electron Microscopy micrographs showing randomly distributed matrix cracks after minicomposite failure.

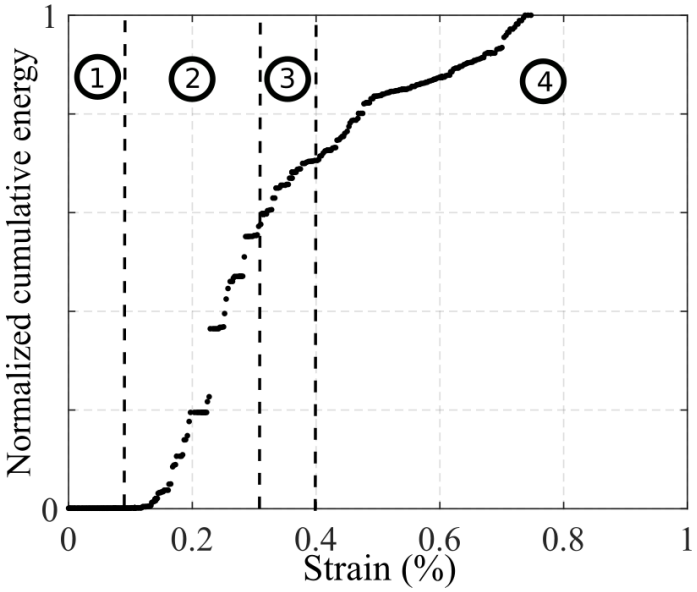

(a) M1 (Hi-Ni-S Fibres)

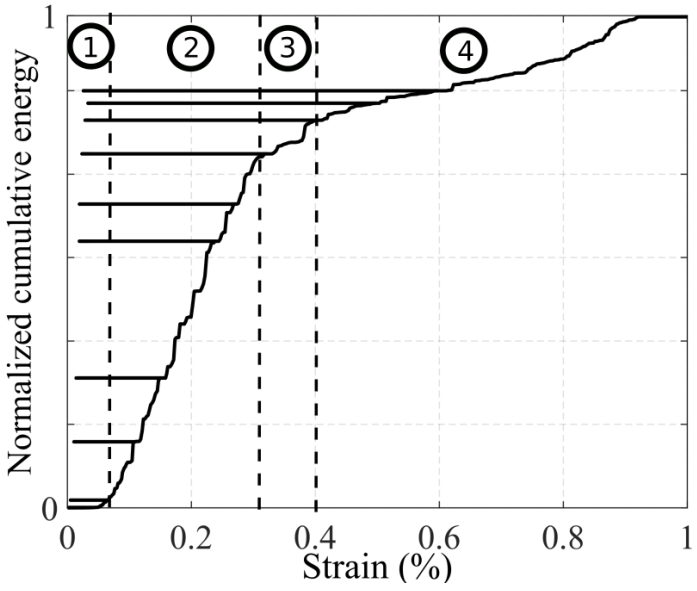

(b) M2 (Hi-Ni Fibres)

Figure 12: Dimensionless acoustic emission cumulative energy during axial tensile tests.

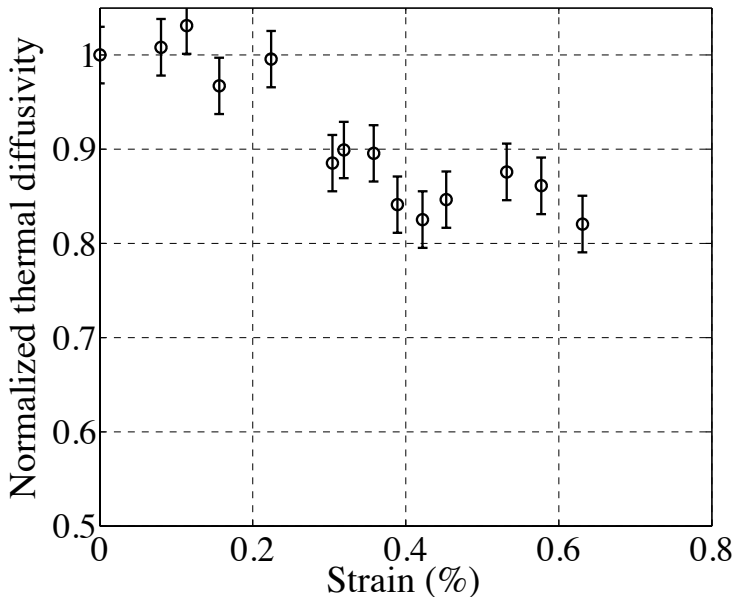

(a) M1 (Hi-Ni-S fibres)($a_o = 11mm^2.s^{-1}$)

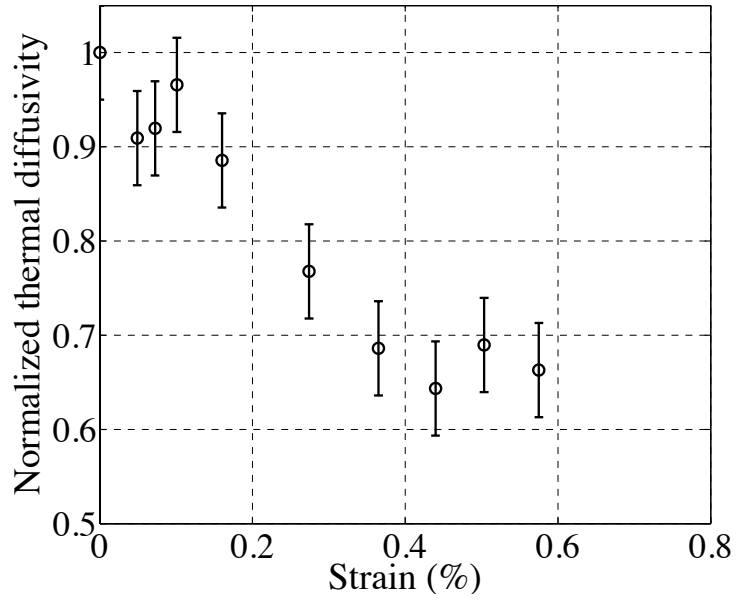

(b) M2 (Hi-Ni fibres) ($a_o = 6.2mm^2.s^{-1}$)

Figure 13: Evolution of the longitudinal thermal diffusivity of minicomposites measured during axial tensile tests.

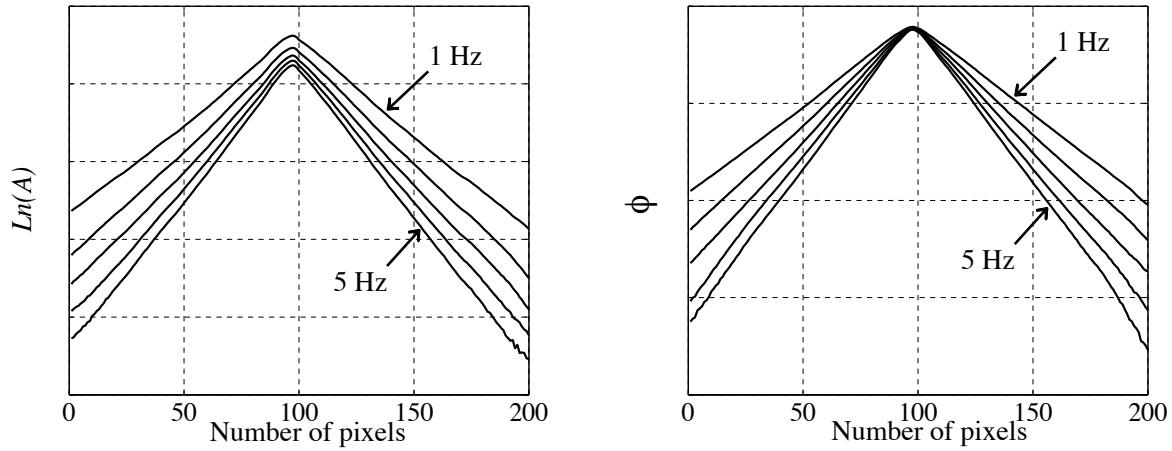

(a) (b)

Figure 14: Profiles of amplitude (a) and phase difference (b) along a cracked minicomposite, for frequencies ranging from 1Hz to 5Hz.

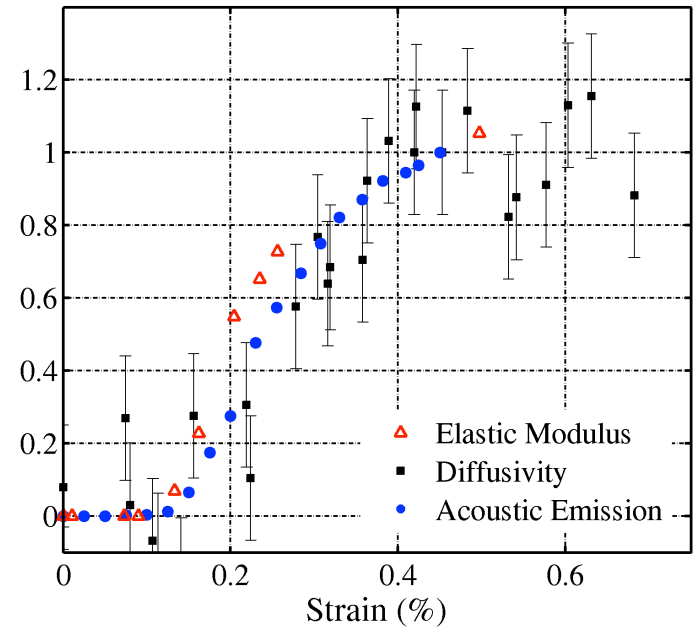

(a) M1 (Hi-Ni-S fibres)

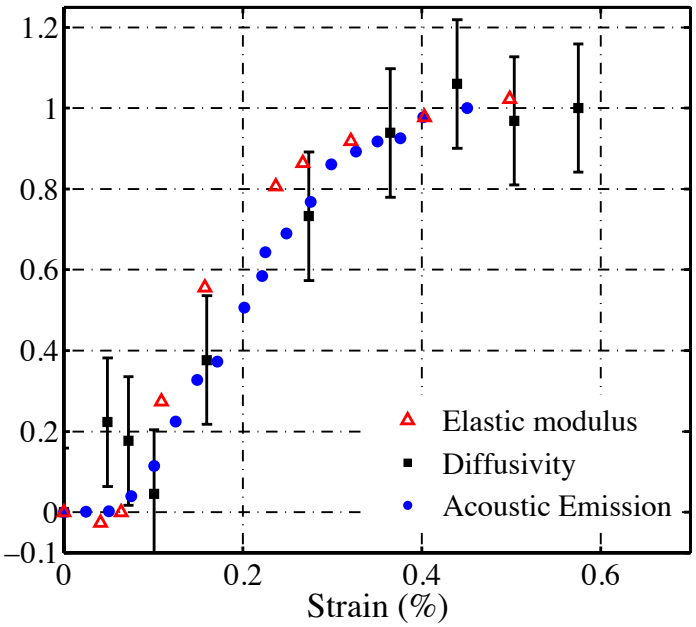

(b) M2 (Hi-Ni fibres)

Figure 15: Comparison of damage indicators derived from elastic modulus, thermal diffusivity and acoustic emission during axial tensile tests.

References

[1] Jones, R., Steiner, D., Heinisch, H., Newsome, G., Kerch, H.. Radiation resistant ceramic matric composites. J Nucl Mater 1997;245:87–107.

[2] Youngblood, G., Senor, D., Jones, R., Graham, S.. The transverse thermal conductivity of 2d-sic/sic composites. Comp Sci Tech 2002;62:1127–1139.

[3] Dumaz, P., Allègre, P., Bassi, C., Cadiou, T., Conti, A., Garnier, J., et al. Gas-cooled fast reactors - status of cea preliminary design studies. Nucl Eng Design 2007;245:1618–1627.

[4] Meyer, M., Fielding, R., Gan, J.. Fuel development for gas-cooled fast reactors. J Nucl Mater 2007;371:281–287.

[5] Zinkle, S., Busby, J.. Structural materials for fission and fusion energy. Mater Today 2009;12:12–19.

[6] Balageas, D., Déom, A., Boscher, D.. Characterization and nondestructive testing of carbon-epoxy composites by a pulsed photothermal method. Mater Eval 1987;45:456–465.

[7] Palumbo, D., Tamborrino, R., Galietti, U., Aversa, P., Tatì, A., Luprano, V.. Ultrasonic analysis and lock-in thermography for debonding evaluation of composite adhesive joints. NDT E Inter 2016;78:1–9.

[8] Barus, M., Welemane, H., Nassiet, V., Pastor, M., Cantarel, A., Collombet, F., et al. Ndt-based design of joint material for the detection of bonding defects by infrared thermography. NDT E Inter 2018;93:157–163.

[9] Bhatt, R., Choi, S., Cosgriff, L., Fox, D., Lee, K.. Impact resistance of environmental barrier coated sic/sic composites. Mater Sci Eng A 2008;476:8–19.

[10] Meola, C., Boccardi, S., Carlomagno, G., Boffa, N., Ricci, F., Simeoli, G., et al. Impact damaging of composites through online monitoring and non-destructive evaluation with infrared thermography. NDT E Inter 2017;85:34–42.

[11] Addepalli, S., Zhao, Y., Roy, R., Galhenege, W., Colle, M., Yu, J., et al. Non-destructive evaluation of localised heat damage occurring in carbon composites using thermography and thermal diffusivity measurement. Measurement 2019;131:706–713.

[12] Kordatos, E.Z., Aggelis, D.G., Matikas, T.E.. Monitoring mechanical damage in structural materials using complimentary nde techniques based on thermography and acoustic emission. Comp Part B 2012;43:2676–2686.

[13] Dassios, K.G., Kordatos, E.Z., Aggelis, D.G., Matikas, T.E.. Crack growth monitoring in ceramic matrix composites by combined infrared thermography and acoustic emission. J Am Ceram Soc 2014;97:251–257.

[14] Bhatt, H., Donaldson, K., Hasselman, D., Bhatt, R.. Role of the interfacial thermal barrier in the effective thermal diffusivity/conductivity of sic-fiber-reinforced reaction-bonded silicon nitride. J Am Ceram Soc 1990;73:312–316.

[15] McDonald, K., Dryden, J., Zok, F.. Effects of matrix cracks on the thermal diffusivity of a fiber-reinforced ceramic composite. J Am Ceram Soc 2001;84:2015–2021.

[16] Hasselman, D., Venkateswaran, A., Tawil, H.. Role of interfacial debonding and matrix cracking in the effective thermal diffusivity of sic-fibre-reinforced chemical vapour deposited sic matrix composites. J Mater Sci Lett 1991;10:1037–1042.

[17] Krapez, J., Spagnolo, L., Frieb, M., Maier, H., Netter, F.. Measurement of in-plane diffusivity in non homogeneous slabs by applying flash thermography. Int J Thermal Sci 2004;43:967–977.

[18] Bamford, M., Batsale, J., Fudym, O.. Nodal and modal strategies for longitudinal thermal diffusivity profile estimation: Application to the non destructive evaluation of sic/sic composites under uniaxial tensile tests. Infrared Phys Technol 2009;52:1–13.

[19] Farooki, J., Sheikh, M.. Finite element modelling of thermal transport in ceramic matrix composites. Comp Mater Sci 2006;37:361–373.

[20] McDonald, K., Dryden, J., Majumdar, A., Zok, F.. Thermal conductance of delamination cracks in fiber-reinforced ceramic composites. J Am Ceram Soc 2000;83:553–562.

[21] Dryden, J., Zok, F.. Thermal phase lag in a solid containing periodic planar cracks. Int J Heat Mass Trans 2001;44:4035–4046.

[22] Dryden, J., Zok, F.. Thermal resistance of bridged cracks in fiber-reinforced ceramic composites. J App Phys 2001;89:4599–4611.

[23] Dryden, J., Deakin, A., Zok, F.. Effect of cracks on the thermal resistance of aligned fiber composites. J App Phys 2002;92:1137–1142.

[24] Aveston, J., Cooper, G., Kelly, A.. Single and multiple fracture. In: The Properties of Fiber Fiber Composites Conference Proceedings of The National Physical Laboratory, IPC Science and Technology Press. Surrey, England; 1971,.

[25] Cao, H., Bischoff, E., Sbaizero, O., Ruhle, M., Evans, A., Marshall, D., et al. Effect of interfaces on the properties of fiber-reinforced ceramics. J Am Ceram Soc 1990;73:1691–1699.

[26] Guillaumat, L., Lamon, J.. Fracture statistics applied to modelling the non-linear stress-strain behavior in microcomposites:influence of interfacial parameters. Int J Fract 1996;82:297–316.

[27] Guillaumat, L., Lamon, J.. Probabilistic-statistical simulation of the non-linear mechanical behavior of a woven sic/sic composite. Comp Sci Tech 1996;56:803–808.

[28] Lissart, N., Lamon, J.. Damage and failure in ceramic matrix minicomposites: experimental study and model. Acta Mater 1997;45:1025–1044.

[29] Naslain, R., Lamon, J., Pailler, R., Bourrat, X., Guette, A., Langlais, F.. Micro/minicomposites: a useful approach to the design and development of non-oxyde cmcs. Composites: Part A 1999;30:537–547.

[30] Lamon, J.. Micromechanics-based approach to the mechanical behavior of brittle matrix composites. Comp Sci Tech 2002;61:2259–2272.

[31] Pailler, F., Lamon, J.. Micromechanics based model of fatigue/oxidation for ceramic matrix composites. Comp Sci Tech 2005;65:369–374.

[32] Laforet, A.. Rupture différée en fatigue statique, aux très hautes températures (800^oc-1300^oc) des fils hi-nicalon, des composites hi-nicalon pyc/sic et des composites hi-nicalon pyc/b4c. Phd thesis; University of Bordeaux; 2009.

[33] El Yagoubi, J., Lamon, J., Batsale, J.C., Le Flem, M.. Model of the influence of damage on the thermal properties of ceramic matrix composites. Ceramic Engineering and Science Proceedings 2010;31:361–372.

[34] Gauthier, W.. Delayed failure at intermediate temperatures (<800^oc) of sic-based tows and filaments. Phd thesis; Bordeaux University; 2007.

[35] Clerjaud, L., Pradere C. Batsale, J., Dihaire, S.. Heterodyne method with an infrared camera for the thermal diffusivity estimation with periodic local heating in a large range of frequencies (25 hz to upper than 1 khz). Qirt J 2010;7:115–128.

[36] Angström, A.. Bestimmung der warme leitung durch periodische temperaturanderung. Annalen der Physikund Chemie 1861;114:513–530.

[37] King, R.. A method of measuring heat conductivities. Phys Rev 1915;6:437–445.

[38] Preston, T.. Theory oh Heat. London: Macmillan Company; fourth ed.; 1929, p. 627.

[39] Starr, C.. An improved method for the determination of thermal diffusivities. Rev Sci Instrum 1937;8:61–64.

[40] Pradère, C., Goyhénèche, J., Batsale, J., Dilhaire, S., Pailler, R.. Thermal diffusivity measurements on a single fiber with microscale diameter at very high temperature. Int J Therm Sci 2006;45:443–451.

[41] Lamon, J., Rebillat, F., Evans, A.. Microcomposite test procedure for evaluating the interface properties of ceramic matrix composites. J Am Ceram Soc 1995;78:401–405.

[42] Lamon, J.. Ceramic Matrix Composites: Materials, Modeling and Applications; chap. Influence of interfaces and interphases on the mechanical behavior of fiber-reinforced ceramic cereamic matrix composites. John Wiley and Sons; 2014, p. 40–64.

[43] Marshall, D., Cox, B., Evans, A.. The mechanics of matrix cracking in brittle-matrix fiber composites. Acta Metall 1985;33:2013–2021.

[44] El Yagoubi, J.. Effet de l'endommagement mécanique sur les propriétés thermiques de composites à matrice céramique : approche multiéchelle. Phd thesis; University of Bordeaux; 2011.

[45] Droillard, C., Lamon, J.. Fracture toughness of 2d woven sic/sic cvi-composites with multilayered interphases. J Am Ceram Soc 1996;79:849–858.

[46] Dong, S., Chollon, G., Labrugère, C., Lahaye, M., Guette, A., Bruneel, J., et al. Characterization of nearly stoichiometric sic ceramic fibers. J Mat Sci 2001;36:2371–2381.

[47] Yamada, R., Igawa, N., Taguchi, T., Jitsukawa, S.. Highly thermal conductive, sintered sic fiber-reinforced 3d-sic/sic composites: experiments and finite-element analysis of the thermal diffusivity/conductivity. J Nucl Mater 2002;307:1215–1220.

[48] Sauder, C.. Effect of irradiation on sic fibres. Internal report; LCTS; 2004.

Matrix cracking